Understanding Lithium Deposition in Lithium-Ion Batteries: The Link between Impedance Results and Electrochemical Behavior

Journal of The Electrochemical Society, 2025 **172** 090523

Understanding Lithium Deposition in Lithium-Ion Batteries: The Link between Impedance Results and Electrochemical Behavior

Andrea Kinberger,[1,2,z] Tom Rüther,[1,2] Leonard Jahn,[1,2] and Michael A. Danzer[1,2]

[1] *University of Bayreuth, Chair of Electrical Energy Systems (EES), Bayreuth, 95447 Bavaria, Germany*
[2] *Bavarian Center for Battery Technology (BayBatt), Bayreuth, 95447 Bavaria, Germany*

Metallic lithium deposition (LD) is the key limiting factor for fast-charging of lithium-ion batteries, as it affects both safety and durability. The reliable detection of LD requires simple and rapid diagnostics, which has led to a widespread adaption of impedance-based LD detection methods in the literature. Most of these studies are largely phenomenological, offering limited insight into the underlying physicochemical mechanisms reflected in the impedance response. In contrast, this study takes an experimental approach by placing the cell under conditions where lithium deposition occurs as the main reaction. Thereby, a targeted analysis of its impact on impedance is enabled by slowly and homogeneously overcharging a graphite anode, which is combined with an oversized cathode in a three-electrode configuration. The setup allows to create controlled conditions from intercalation via the onset of LD to exclusively LD. The electrodes are analyzed using operando and ex-operando impedance measurements. Additionally, a distribution of relaxation times analysis is performed to gain deeper insight into the electrochemical processes under different LD conditions. This work thus bridges the gap between phenomenological detection methods and the fundamental understanding of LD, offering potential for an improved detection and prevention of LD and ultimately fast-charging of lithium-ion batteries.

 [DOI: 10.1149/1945-7111/ae0073]

Manuscript submitted May 26, 2025; revised manuscript received August 12, 2025. Published September 19, 2025.

Lithium-ion batteries (LIBs) have become indispensable in multiple applications spanning from power tools and home energy storage to large-scale grid-integrated storage solutions.[1,2] Driven by the rapid market expansion over the past decade, their critical role in electromobility has gained particular attention.[3,4] Despite significant advances, the comparatively long charging times relative to refueling conventional vehicles remain a key barrier to a broader adaption of electric vehicles.[5] The fast charging capability of LIBs is limited by the kinetics of the electrochemical processes at the anode. If the local anode potential on a particle surface drops below 0 V vs the reduction potential of Li/Li^+, metallic lithium deposition (LD) becomes thermodynamically possible.[6–8] This limitation becomes particularly pronounced at high states of charge (SoC),[6,7,9,10] where the anode potential decreases due to the increasing intercalation of lithium ions into the anode active material. The issue is further exacerbated under conditions associated with elevated overpotentials, such as low temperatures[6,7,11,12] and high current rates.[9,11,13,14] LD is partially reversible if the deposition takes place within the solid electrolyte interphase (SEI). In this case, the deposited lithium can be recovered again by stripping processes.[15] Under prolonged LD conditions, irreversible LD may occur when the deposition extends beyond the SEI, enabling chemical reactions with the electrolyte that form irreversible products or when lithium metal becomes electronically isolated and thus electrochemically inaccessible. This process effectively removes lithium from the cell's inventory, resulting in capacity loss and increased internal resistance. The morphology and surface area of the LD can vary significantly. In the worst case scenario, lithium metal forms high-surface area dendrites that may grow through the separator, leading to internal short circuits and posing risk of thermal runaway.[16,17] It is therefore essential to develop reliable, non-destructive methods for the early detection of LD,[7,10] enabling adaptive load profiles to ensure safe operation and high cycle stability of LIBs.

Multiple fingerprints of reversible LD can be detected using nondestructive methods by observing measurable battery variables after charging. Among these, the post-charging voltage profile serves as a key indicator, as the lithium stripping process leads to a characteristic voltage plateau.[10,15,18–21] Furthermore, the effect of LD is reflected in the relaxation behavior of cell expansion after charging and has been shown to be a reliable method for LD detection.[22–25] As demonstrated by Jahn et al.,[23] combining this approach with voltage signals further improves detection sensitivity and robustness. A similar effect can also be observed in impedance measurements during the relaxation phase, where deviations from the expected exponential behavior of the impedance magnitude within the SEI frequency range serves as indicator of LD.[6,9] However, these methods are retrospective in nature, detecting LD only after it has occurred during the previous charging cycle. Consequently, the onset of LD cannot be identified and real-time monitoring or control is not possible.

For this reason, operando methods are needed and both voltage[26–28] and dilatation[29,30] signals have been utilized to detect the onset of LD. In addition approaches based on internal resistance and impedance measurements have proven effective in identifying LD.[12,31,32] Despite their effectiveness, these methods typically require current interruptions, which influence the charging profile and prolong the overall charging time, thereby reducing their practicality for real-time monitoring in fast-charging scenarios. To overcome this issue operando impedance methods superimpose sinusoidal signals onto the charging current. This allows the LD onset to be detected without interruption. However, from a mathematical point of view, the operando measurement poses challenges. In general, the impedance analysis is based on the assumption of a linear, time-invariant system, whereas the battery undergoes dynamic, nonlinear processes during charging. In particular, changes in SoC lead to time- variance and high charging currents lead to a nonlinear battery behavior complicating the interpretation of the impedance data. Despite these challenges, feature-based detection of LD using operando impedance measurements has become well established in the literature.[7,33–40] A reduction in the real part of the impedance is regarded as a particularly reliable indicator for the onset of LD in both full and half cell configurations.[7,33–35] Initial attempts have been made to analyze the underlying processes responsible for this impedance drop, aiming to understand why LD manifests as such in operando measurements. According to Koseoglou et al.[33] and Keilhofer et al.[39] the observed impedance drop can be attributed to a reduction in charge-transfer resistance. Koleti et al.[41] propose that this reduction may result from a redistribution of the reaction current, which, after the onset of LD,

[z] E-mail: Andrea.Kinberger@uni-bayreuth.de

is no longer solely directed toward intercalation but is partially diverted to lithium deposition. In addition, Katzer et al.[7,35] suggest that short-circuiting of the SEI due to LD may also contribute to the impedance drop. However, a direct validation of the process assignment is still pending. Furthermore, the aforementioned studies that detected LD using sinusoidal currents were conducted at high currents and/or low temperatures to rapidly induce LD. Due to kinetic limitations, inhomogeneous conditions prevail within the cell, leading to the simultaneous occurrence of LD and intercalation reactions. Particularly in experiments with commercial full cells, the temperature change caused by the charging process can also affect the impedance behavior. A study by Jiang et al.[42] investigated the relationship between LD and operando impedance by examining both controlled overcharging and fast-charging scenarios in half-cell configurations. These experiments employed lithium-metal counter electrodes, which may have influenced the impedance response due to their own dynamic behavior.[43] The study identified a correlation between the anode potential and the characteristic bending of the impedance curve at the onset of LD. However, it did not establish a direct link between the operando impedance features and specific electrochemical processes, for example through comparison with ex-operando electrochemical impedance spectroscopy (EIS) or process assignment. Therefore, this work addresses this gap by systematically comparing operando impedance measurements with ex-operando EIS, in order to validate the physical origin of the observed impedance features associated with LD. An experimental cell setup with an overdimensioned cathode is used to homogeneously overcharge a graphite anode and observe changes from lithium intercalation, via the onset of LD, to exclusively LD reactions. This work has the following goals:

- deepen the understanding of mechanisms involved in LD.
- gain detailed insights in the impedance behavior, from intercalation via LD onset to exclusively LD conditions.
- systematically study the underlying electrochemical processes through a distribution of relaxation times (DRT) analysis.
- enable a process assignment of operando impedance signals and a validation using ex-operando EIS measurements.
- provide an experimental design that enables the extraction of equivalent circuit model parameters for both intercalation and LD reactions using EIS data, which can be used in future studies to simulate the current distribution of LD reactions in physicochemical battery models.

Material and Methods

Cell assembly and formation.—For a slow, homogeneous overcharging of the anode a lithium reservoir exceeding the capacity of the negative electrode is needed. Similar experiments are usually done by building cells with a lithium metal counter-electrode. As shown by Rüther et al.[43] the high impedance of the lithium metal counter electrode cannot be neglected in EIS measurements, even when using a reference electrode. To avoid this issue while characterizing the influence of LD on the impedance behavior of Li-ion battery cells, experimental cells are built with an oversized cathode instead, to ensure homogeneous overcharge and therefore LD conditions in the anode. The setup is shown schematically in Fig. 1.

Electrode materials with different capacities are used in a laboratory test cell setup (EL-Cell ECC-PAT-Core, 18 mm electrode diameter). Electrode sheets, provided by CustomCells, are punched into 18 mm diameter discs. For the anode a graphite electrode with an areal capacity of 1.2 mA h cm^{-2} is used. The high-power anode is combined with a high-energy NMC811 cathode with a areal loading of 3.5 mA h cm^{-2}. This setup ensures the possibility to overcharge the anode, whereby the cathode is not overdischarged at its maximum capacity. Anode and cathode are separated by a Whatman GF/A glass fiber separator, incorporating a reference

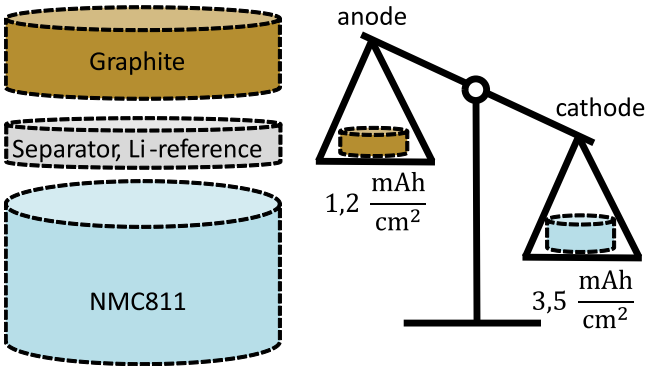

Figure 1. Schematic illustration of the three-electrode setup.

electrode via pre-assembled separator–reference ring units supplied by EL-Cell to enable half-cell potential measurements. The reference ring setup is chosen for easy and reproducible cell assembly, minimizing variability between measurements. However, although a slight influence on the impedance response cannot be entirely excluded, comparison with full-cell and cathode-only impedance spectra (see Appendix A) confirms the absence of major artifacts. 100 µL LP57, a solution of 1 mol $LiPF_6$ in a 3:7 v/v mixture of EC and EMC, provided by Gotion, is used as the electrolyte. The cells are built in a glove box under argon atmosphere.

After cell assembly the cells are stored for 24 h in a climate chamber, which is maintained at 25 °C by a Huber CC-515 circulation thermostat, under argon atmosphere. All following tests including the formation and cell testing are carried out under these ambient conditions using a Biologic VMP300 potentiostat. The formation of the cells is done according to the data sheet of the electrodes with small adaptions due to the uneven capacities of anode and cathode. In the first two cycles, a constant current constant voltage (CCCV) charging protocol is applied, with a C-rate of C/10 during the CC-phase. The initial C-rate for the formation steps is calculated based on the nominal capacity of the anode, scaled to the electrode area. The CC phase is terminated once the anode potential drops below 0.01 V, followed by a CV-step, which continues until the current falls below C/100. Discharging is performed using a CC-step at C/10 until the anode voltage reaches 1.0 V, followed by a 10 s CV-step. After a rest period of 10 min, the cycle is repeated once. In the following two cycles CCCV charging and discharging is performed at a constant current of C/5 with a cutoff criterion of C/50 in the CV-phase of the charge. To further precondition the cells, an additional 15 cycles are run in the CCCV process at a C-rate of C/5 and a CV cutoff criterion of C/10 to ensure that all formation processes are complete and the cells have stable cycle performance. The cells anode capacity, which is used in the further experiments to set the C-rate, is determined using the last charging cycle.

Impedance analysis.—To reveal the influence of LD on the impedance behavior, EIS measurements are recorded at short intervals during slow, gradual overcharging. In addition, a second series of measurements with superimposed sinusoidal currents on the charging current is recorded in order to gain real-time insights into the polarization behavior during battery operation. For each measurement, a new cell is used to ensure reproducibility and to avoid cumulative effects from previous LD.

Electrochemical impedance analysis.—EIS spectra are subsequently measured at 37 grid points during slow rate charging. For a familiar representation, the charge throughput is normalized to the anode capacity determined during the last formation cycle (CCCV cycling from 1.0 V to 0.01 V with a CV determination criterion of C/10). For this reason, all SoC values given refer to the anode capacity and can reach values of more than 100 % in the event of overcharging. Starting from 0 % SoC at an anode potential of 1.0 V each

SoC step is approached with a charging C-rate of C/10 followed by a 3 h relaxation phase before the EIS measurement is carried out. Until 90 % SoC, 10 % capacity steps are made to reduce the measurement duration, at the expected onset point of LD the step width is reduced to 0.5 % SoC to achieve a high resolution of possible changes in the impedance behavior. Preliminary tests revealed the approximate onset point of LD within this SoC window, guiding the selection of the region with higher measurement resolution. The step width is increased again at high SoC when the transition from intercalation to LD conditions is expected to be completed. The EIS measurement is conducted at ten frequency points per decade between 1 kHz and 100 mHz. To avoid misunderstandings regarding the electrochemical designations of the electrode polarities, all impedance values in this paper are those of the graphite anode. The parameters of the EIS measurement can be found in Table I.

A Kramers-Kronig test is conducted to asses the validity of the measured impedance spectra with respect to linearity and stationarity. To prevent overfitting, the extended Kramers-Kronig method by Plank et al.[44] is employed. Further details on the test are available in the literature.[44–48]

Distribution of relaxation times analysis.—For the post processing of the EIS-data the distribution of relaxation times methods (DRT) is used to convert the frequency-domain data into a time-domain function, enabling the identification, separation, and quantification of underlying processes. The DRT is obtained using the discrete and regularization-based deconvolution approach of the generalized DRT method introduced by Danzer.[49] Following the recommendation by Hahn et al.,[50] the number of time constants is set to three times the number of measured frequency points. Additionally, to ensure smooth behavior at the boundaries, the limits of the time constants are extended by one decade beyond the highest and lowest measured frequencies.[45] The regularization parameter is kept constant at $\lambda = 0.4$ to ensure better comparability across all measurements. Although this value is slightly higher than that obtained using the L-curve method ($\lambda_L = 0.2$) introduced by Paul et al.,[51] it facilitates the smoothing of the distribution function. This smoothing is particularly useful for the interpretation in this study, as it contributes to reducing the impact of high noise levels and cell-to-cell variations in the experimental EL-Cell configuration. Further information on the calculation[45,49,52] or interpretation[43,45] of the DRT can be found in the literature.

Operando impedance analysis.—For the operando impedance measurements sinusoidal currents with different frequencies are superimposed on the charging current. Thus, the experimental procedure leads to a nonlinear behavior and a change in the battery's SoC, contrary to the stationarity and linearity criteria of electrochemical impedance spectroscopy.[53,54] The non-linear operando impedance measurement nevertheless shows characteristic changes in the electrochemical behavior, which can be a clear indication of LD. By validating the data with ex-operando measurements, a more comprehensive process analysis can be made, enhancing the understanding of the underlying mechanisms. To maximize the resolution of the time-varying impedance, a reduced spectrum consisting of eight logarithmically distributed frequency points between 10 kHz and 0.5 Hz is recorded. By reducing the number of frequency points to eight frequencies, a repetition can be carried out every 8 s, which corresponds to a SoC change of only 0.02 % in case of a DC offset of C/10. The spectrum is repeatedly recorded until 120 % SoC is reached. The amplitude of the AC-current is set to 250 µA, in order to not reverse the current sign at any time at a charging current of C/10. The operando impedance measurement is conducted for a charging current of C/10 and for a charging current of C/2. To exclude the influence of previous LD processes, a fresh cell is used for each measurement. A total of three cells with C/10 and two cells with C/2 underwent operando-EIS.

Results and Discussion

Assignment of characteristic impedance features and process analysis of metallic lithium deposition via impedance spectroscopy.— *Fingerprints of metallic lithium deposition in the frequency domain.*—Figure 2a shows the Nyquist plot of the anode impedance measurements of one measured cell in the SoC range between 10 % and 119 %. The results of the associated extended Kramers-Kronig test can be found in Appendix D. To show the reproducibility of the experiment, the Nyquist plots for two further cells are shown in Appendix F. In Fig. 2b, the width of the characteristic semicircle w_{RQ} is shown for each SoC point. The width is determined as a geometric feature, calculated from the difference in real part values between the first measurement point at 1 kHz and the low frequency minimum located in the lower two-digit down to the single-digit hertz range. In Fig. 2c the height h_{RQ} is shown, which corresponds to the minimum of the imaginary part within the semicircle region. In the SoC range from 10 % to 96 % a systematic reduction in both the diameter w_{RQ} and the height h_{RQ} of the depressed semicircle, which represents SEI, charge transfer, and double layer effects, is visible. This trend is attributed to a decrease in charge transfer resistance with increasing SoC.[55] As in this region the anode potential has not fallen below 0 V vs Li/Li^+, it is concluded that LD criteria are not fulfilled and no LD has occurred. The change in impedance cannot be attributed to the altered charging step duration at SoCs of 90 % and 94 % as the initial measurement points with finer resolution do not yet indicate any change in impedance behavior. Starting at a SoC of 96 %, slightly before reaching the full anode capacity, a more pronounced change in the Nyquist plot is observed, characterized by a substantial reduction in both the diameter w_{RQ} and height h_{RQ} of the depressed semicircle. This behavior can be linked to the onset of LD, as once LD is thermodynamically possible, the current density of the intercalation reaction is expected to decrease. Li^+ ions are deposited directly as elemental lithium (Li^0) on the anode surface and the current density is split between intercalation and LD reaction. As the charge transfer resistance of the LD reaction is assumed to be lower than the charge transfer resistance of the intercalation reaction,[35,56] this is visible as a reduction of the semicircle dimensions in the Nyquist plot. In our experiment 96 % SoC was therefore determined as first LD onset point, because a characteristic change in impedance behavior becomes visible at this point. The sharp decline of the semicircles width and height continues up to a SoC of 106 %, beyond which the rate of decrease slows. The further impedance decline in the semicircle at SoCs >106 % can be attributed to an increasing active surface area of the metallic lithium[35] and therefore a reduced resistance with increasing charge throughput. However, the slowing rate of decline in this region is further analyzed in Section *Process analysis of metallic lithium deposition*. In the low-

Table I. Overview of EIS and operando impedance measurement settings.

Method	Frequency	Amplitude in µA	Relaxation time in h	SoC gridpoints in %
EIS	10 steps/decade in [1 kHz −100 mHz]	300	3	$0 \xrightarrow{10} 90$: intercalation $94 \xrightarrow{0.5} 104$: LD onset $106.5 \xrightarrow{2.5} 118.5$: LD region
operando impedance	8 points in [10 kHz−100 mHz]	250	–	–

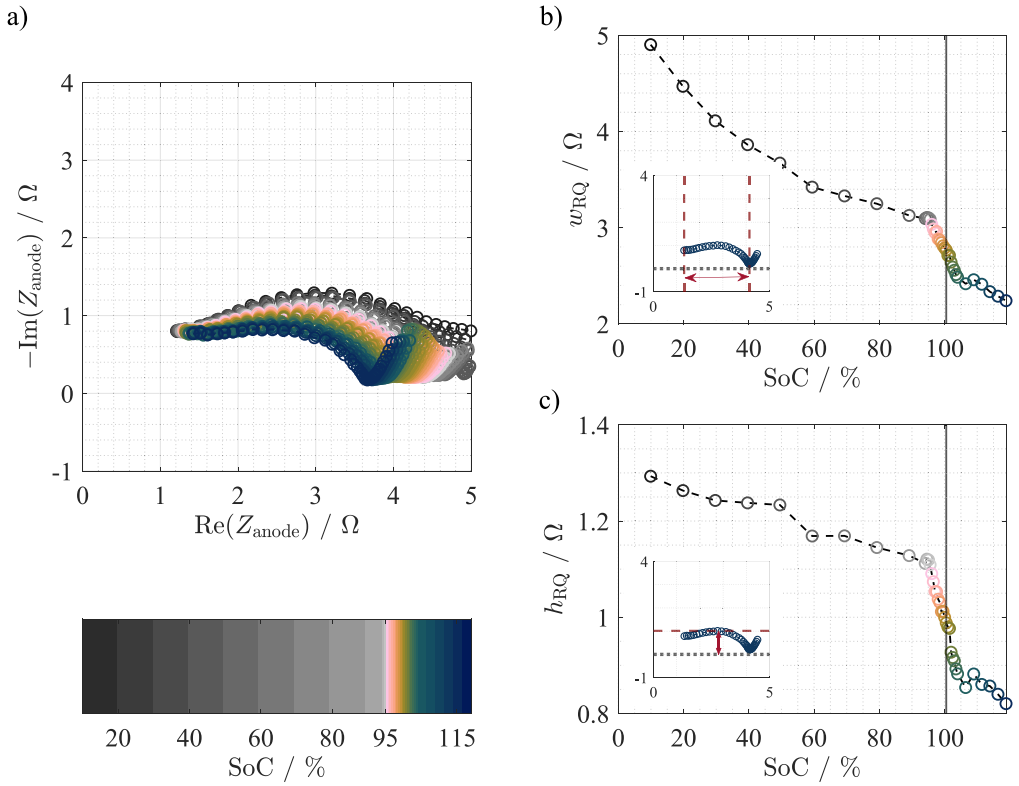

Figure 2. Nyquist plots of the anode impedance of an experimental cell for different SoCs in a frequency range between 1.0 kHz and 0.1 mHz in (a). The color map indicates the SoC of the anode.. Plot (b) show the width of the RQ-semicircle and plot (c) the height of the RQ-semicircle. The solid line in plot (b) and (c) marks 100 % SoC. The inline plots in (b) and (c) illustrate the evaluation principle by showing how the width w_{RQ} and height h_{RQ} of the RQ-semicircle are determined.

frequency domain, a diffusion branch is visible, which becomes longer and steeper in the LD onset region (SoC between 96 % and 106 %). This behavior may be attributed to a reduced interfacial capacitance caused by the deposition of metallic lithium within the SEI. Beyond 106 % SoC, the observed increase of the imaginary component of the diffusion impedance may reflect a shift in the deposition mechanism, potentially caused by LD breaching the SEI and modifying the diffusion processes through the formation of new SEI. In Section *Validation of operando impedance measurements* the comparison with operando impedance measurements serves to identify and discuss possible influences of the rest phases in the ex-operando EIS.

Another option is to look at the progression of individual frequencies, since using a single frequency in the test protocol would be a time-efficient method to detect LD compared to a frequency sweep. In order to find frequencies which are most sensitive for the detection of LD, the course of individual frequency points over the SoC is analyzed. Figures 3b and 3c show the progression of individual frequency points from different characteristic areas of the Nyquist plot. Additionally Fig. 3a provides an overview of their characteristic range in the Nyquist plot. 96 % SoC was identified as the LD onset point by looking at the characteristic features of the Nyquist plot. The real part of the impedance at high frequencies in the first half of the semicircle does not change with the onset of LD at 96 % SoC, but shows the typical bathtub behavior, whereas frequencies near the apex (32 Hz) or near the diffusion minimum (0.5 Hz) show a noticeable change in behavior. From this results, it could be concluded that the charge transfer and the diffusion processes are affected by the onset of LD. A further process analysis is carried out using DRT in the following section. In contrast to the real part of the impedance at 0.5 Hz, the imaginary part starts to increase at the onset point of LD. This behavior results from the steeper diffusion branch, which is caused by the change in diffusion properties from intercalation to LD. These considerations show that frequencies in the area of the charge transfer and on the left side of the diffusion minimum are well suited for the detection of LD. At frequencies in the diffusion branch, only the real part shows the characteristic drop due to the change in slope.

Process analysis of metallic lithium deposition.—For a deconvolution and enhanced characterization of overlapping electrochemical phenomena according to their characteristic relaxation times, a distribution of relaxation times (DRT) analysis is performed. The distribution function of the anode impedance spectrum is illustrated in Fig. 4a. The peaks in the distribution function are attributed to electrochemical processes.This attribution is carried out using the 10 % SoC curve, where four dominant peaks are observed. The assignment to processes is established through analysis of SoC-Śdependent variations. To calculate the area and the height of the peaks, shown in Figs. 4b and 4c, the distribution functions were post-processed using Gaussian peak fitting, following the method described by Hahn et al.[50]. The peak at the lowest time constant, i.e., the highest frequency ($1{\cdot}10^4$ Hz), P_1, occurs at frequencies outside the measurement range and is presumably caused by boundary effects or regularization;[45] since it is also independent of the SoC, it is neglected for the following analysis. Peak P_{SEI}, located at a frequency between 1 kHz and 100 Hz, exhibits a slight dependence on the SoC in the polarization at SoCs below 96 %. However, the corresponding time constant remains largely independent of the SoC across the entire measuring range. Based on its behavior and characteristic frequency, this peak is primarily attributed to processes occurring within the SEI.[43,45] Peak $P_{\mathrm{CT\&DL}}$, located at a frequency of 10 Hz at 10 % SoC, exhibits a strong dependence on the SoC, as reflected in changes in both polarization and frequency. Taking this sensitivity and its characteristic frequency into account, the corresponding process can be attributed to charge transfer and double-layer effects.[43,45,57] In contrast, peak $P_{\mathrm{Diffusion}}$ shows only limited sensitivity to variations in SoC. Together with its characteristic low frequency of 0.8 Hz, this

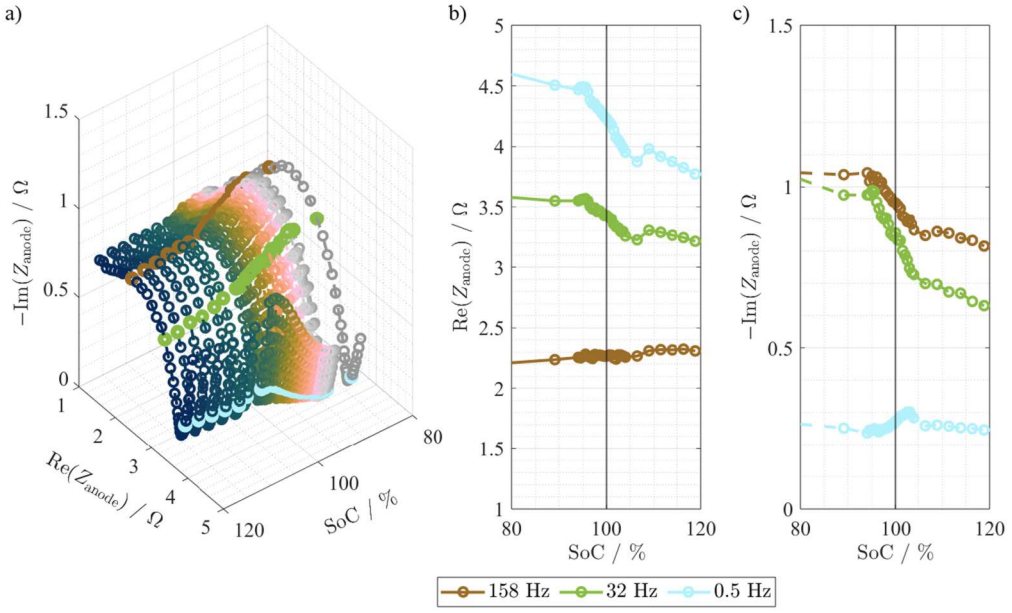

Figure 3. Nyquist plot over SoC as 3D plot between 80 % and 120 % SoC in (a), three frequencies at characteristic geometric positions are marked. On the right side the course of the real part in (b) and of the imaginary part in (c) of the impedance at the three marked frequencies. The dashed line in plot (b) and (c) marks 100 % SoC.

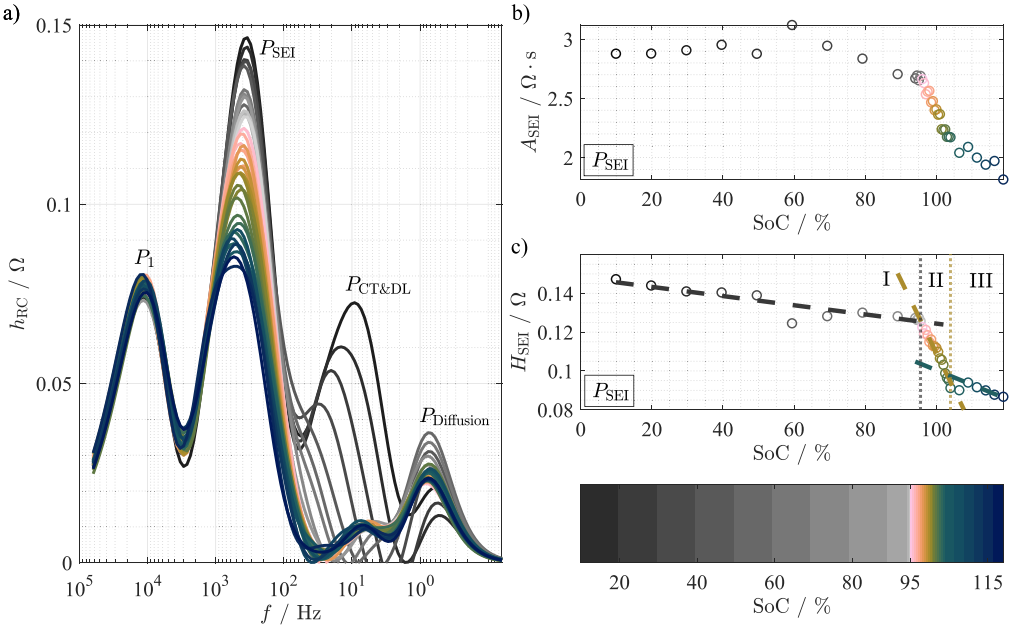

Figure 4. DRT analysis of the EIS measurements in (a). The color map indicates the SoC of the anode.. Plot (b) and (c) show the area and the height of P_{SEI}. In plot (c), the thick dashed lines show the different slopes of the polarization reduction, the vertical dotted lines separate the different LD regions.

behavior is primarily attributed to mass transport and solid-state diffusion processes.[43,45,57]

Investigating the SoC-dependent evolution of individual processes—under conditions ranging from pure intercalation, through the onset of lithium deposition, to predominant lithium deposition—enables a mechanistic interpretation of these processes as a function of the SoC. In the resulting distribution function, individual peaks serve as markers of these distinct processes. The most pronounced SoC sensitivity is exhibited by the charge-transfer and double-layer peak $P_{\mathrm{CT\&DL}}$. With increasing SoC the polarization of the charge transfer and double-layer-related peak decreases significantly, while its frequency shifts to higher values. This indicates a facilitated charge transfer at the electrode surface, which typically occurs at high degrees of lithiation.[58] An analysis solely based on the Nyquist plot could suggest that the onset of LD leads merely to a further reduction in charge-transfer resistance. A similar conclusion was drawn by Chen et al.[56] using DRT analysis. However, in our DRT results, this behavior is not observed, as the polarization associated with the corresponding relaxation process is already comparatively low at higher SoCs, potentially masking any further changes related to the onset of LD. In contrast, a pronounced influence of the LD onset is observed on peak P_{SEI}. Figures 4b and 4c illustrate the evolution of the area and height of peak P_{SEI} evaluated by a peak analysis (MATLAB (R2023b), function *findpeaks*). At an SoC of 96 %, a pronounced decrease in both parameters becomes visible. This point coincides with the previously identified onset of LD.

Having a deeper look at the peak height, three regions with different slopes can be identified: in region I, where intercalation predominates, the peak height changes only slightly; starting at the LD onset point in region II, the polarization is strongly reduced, before the polarization change becomes less pronounced when LD lasts longer (SoC $>$ 106 %) in region III. To guide the eye, the three different gradients resulting from the respective ranges are shown in the plot. A possible explanation for the strong reduction of polarization at the onset point is the deposition of metallic lithium within the SEI, with the effect of an increased SEI conductivity up to a short circuit of the passivation layer.[35] The measurement results showing a reduced SEI peak at the onset of LD are consistent with the DRT findings of Brown et al.[37] during the slow overcharging of a graphite anode. However, contrary to their subsequent interpretation, which suggests an increase in SEI resistance under LD conditions, we cannot confirm such an increase. The lower slope of the polarization curve in the long period of overlithiation may be due to the buildup of new SEI, which suggests that LD occurs outside the SEI.

Assignment of characteristic impedance features of metallic lithium deposition in operando impedance measurements.— *Feature analysis of the impedance components.*—Figures 5a and 5b show the evolution of the real and imaginary part of the anode impedance as a function of the SoC for all frequencies $<$1 kHz during operando impedance measurement for one cell. Although frequencies above 1 kHz are also measured, they are not shown here as they do not make any significant contributions to the observation of LD processes. The data is smoothed using a moving averaging filter to reduce noise and to recognize the underlying trends more clearly. To demonstrate the reproducibility of the findings, the results of additional cells are provided in the Appendix C.

The observed impedance-based LD onset criterion - a decrease in impedance in the low frequency region - occurs at an SoC of 97 %, shortly before the voltage-based LD criterion of 0 V vs Li/Li$^+$ is reached at an SoC of 102 %. In the anode potential curve shown in Fig. 5c, a final potential drop is observed in this SoC range. The potential drop is attributed to the completion of the stage 2 $\rightarrow$ 1 transition of graphite, corresponding to the formation of the fully occupied LiC_6 structure.[59,60] If the cell is charged beyond this point, no further lithium can be intercalated into the graphite. Instead of intercalation, metallic lithium is deposited on the graphite surface. As frequencies below 35 Hz exhibit a strong correlation with the anode potential vs Li/Li$^+$, in both the real and imaginary part of the impedance until the potential minimum is reached, the corresponding drop is also reflected in the in the impedance curves. Shortly after reaching 0 V vs Li/Li$^+$, a potential minimum due to the nucleation drop is observed. The potential of the graphite electrode then gradually increases again and approaches a value close to 0 V vs Li/Li$^+$. This behavior is characteristic for the formation of metallic lithium on the electrode surface.[61] At this point, the intercalation reaction is assumed to be completed and only LD takes place. The impedance in the frequency range sensitive to LD ($<$35 Hz) continues to decrease, which may indicate an increasing area of deposited lithium. This behavior is likely due to lithium preferentially plating onto existing lithium deposits, thereby increasing the effective electrochemical reaction area.[14]

This characteristic impedance drop in the real part is used as a feature to detect the onset point of LD on the particle surfaces in other studies.[7,34,35,39] They identified frequencies in the low-frequency region ($<$100 Hz) that offered good sensitivity for detecting LD, which aligns with our findings. Like in the EIS experiment, the real part of the impedance at high frequencies (in the left half of the semicircle segment of the Nyquist plot) do not change with the onset of LD, e.g. the impedance for frequencies $>$100 Hz remains almost constant over the entire measuring range and is therefore not suitable for the detection of LD.

The operando impedance method used shows changes of the polarization when LD occurs with the advantage of being able to be measured during the charging process without current interruptions. However, the method violates the assumptions of a LTI system, as the cell states - such as concentrations, temperature or electrochemical activity - change dynamically during the measurement. To

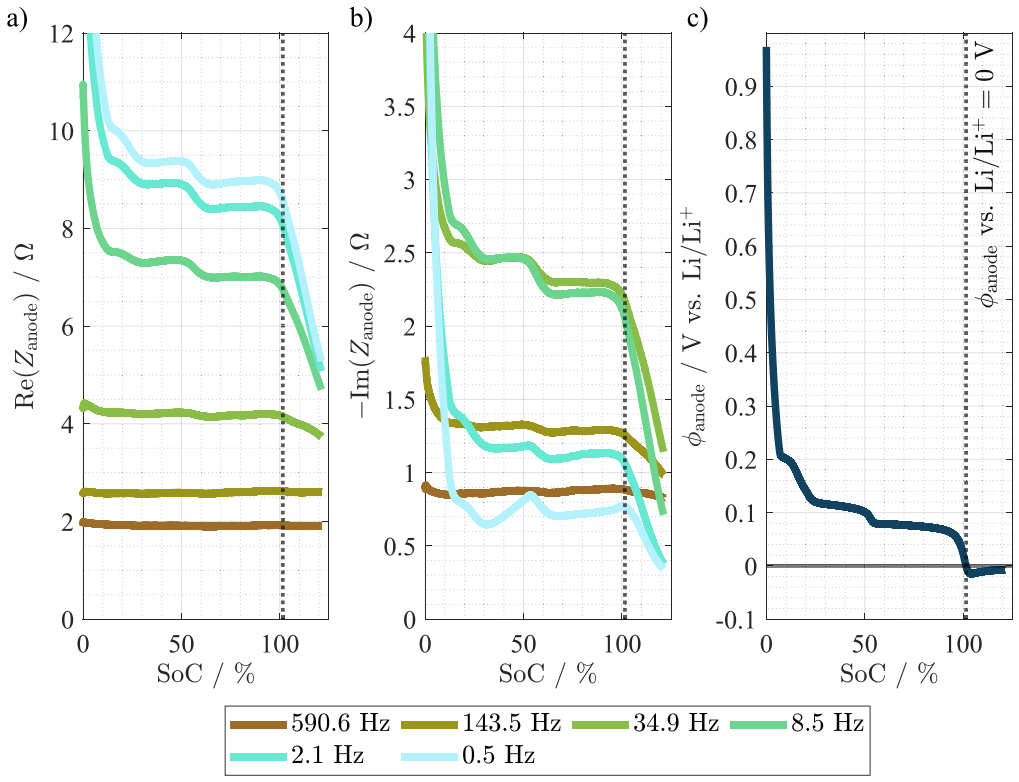

Figure 5. Course of the real part and of the imaginary part of the impedance of all tested frequencies in the operando impedance in (a) and (b). Plot (c) shows the anode potential vs Li/Li$^+$ during the measurement. The dashed lines marks the point where the anode potential vs Li/Li$^+$ reaches 0 V.

validate the feature-based LD detection based on operando impedance measurements a comparison with ex-operando EIS data is carried out.

Validation of operando impedance measurements.—To examine the consistency of changes and the reliability of the operando measurements, a comparison of operando impedance with electrochemical impedance spectroscopy is carried out. In Fig. 6 ex-operando EIS and operando impedance measurement are shown in the Nyquist plot in the conditions from pure intercalation to the onset of LD to mainly LD. Figure 6a shows the Nyquist plot of the EIS. Figure 6b the operando impedance measurements for the same SoC window. Overall, the measured operando impedance is higher than that obtained from EIS. While the absolute values may be influenced by variations in the EL-cells, the observed trend is consistent across all cells used. Additionally, the positions of identical frequency points in the Nyquist plot are shifted slightly toward lower values along the real axis. Therefore, the 0.5 Hz frequency point in the operando measurement is still on the left side of the diffusion branch and is sensitive to the onset of LD, indicated by an impedance drop in the real as well as in the imaginary part.

This behavior is additionally illustrated in Fig. 7, where the real and imaginary parts at different frequencies are plotted versus the SoC. For 0.5 Hz, the operando measurement shows a drop in both the real part and the imaginary part in the LD onset range, whereas the curve of the EIS measurement for the same frequency shows the characteristic drop for the real part due to the steeper diffusion branch only. In the EIS measurement, the impedance at 32 Hz lies in the right half of the semicircle and therefore shows the impedance drop in both the imaginary and the real part. The according 35 Hz point of the operando impedance is close to the maximum of the semicircle and similarly shows sensitivity to LD in both components. High frequencies (590 Hz / 613 Hz) show no impedance drop in either measurement. The LD-related impedance drop at 35 Hz (operando) and 32 Hz (ex-operando EIS) occurs in both cases shortly before reaching 100 % SoC. However, once the minimum of the electrode potential in the operando impedance measurement is reached at around 105 % SoC, a divergent behavior of the operando impedance and the ex-operando EIS data becomes apparent. Specifically, the real and imaginary components of the operando impedance continue to decrease steadily with increasing SoC, whereas the corresponding values from the EIS measurements exhibit only a slight decline beyond 105 % SoC, likely due to the relaxation periods inherent to the EIS measurement protocol. One possible explanation for the observed difference could be that during these rest phases, stripping processes may occur, allowing previously deposited lithium to oxidize and dissolve back into the electrolyte[56] or to re-intercalate in directly adjacent graphite particles.[62] As a result, the amount and area of LD would be lower compared to the operando measurements. In addition, during the rest periods, the freshly formed SEI layers around the deposited lithium may undergo further structural and compositional changes,[63] which may influences the impedance.

Experimental use of operando impedance for the definition of charging limits in a parameter table.—To ensure safe and efficient charging of lithium-ion batteries and to prevent LD, the maximum permissible charging currents must be precisely defined in advance. The current limits during charging are determined using experimental tests, physical-electrochemical models, data-based methods or a combination thereof.[64] The impedance-based method can provide a fast experimental approach to determine the LD onset for different C-rates. The first derivative of the real part of the impedance is an often used feature to detect the onset of LD,[35,39] as changes are more clearly visible. In Fig. 8 the first derivative of the real part of the impedance curve for 0.5 Hz over SoC is shown for charging with C/2 in comparison to the slow charging with C/10. A new cell was used for the C/2 tests to exclude differences due to

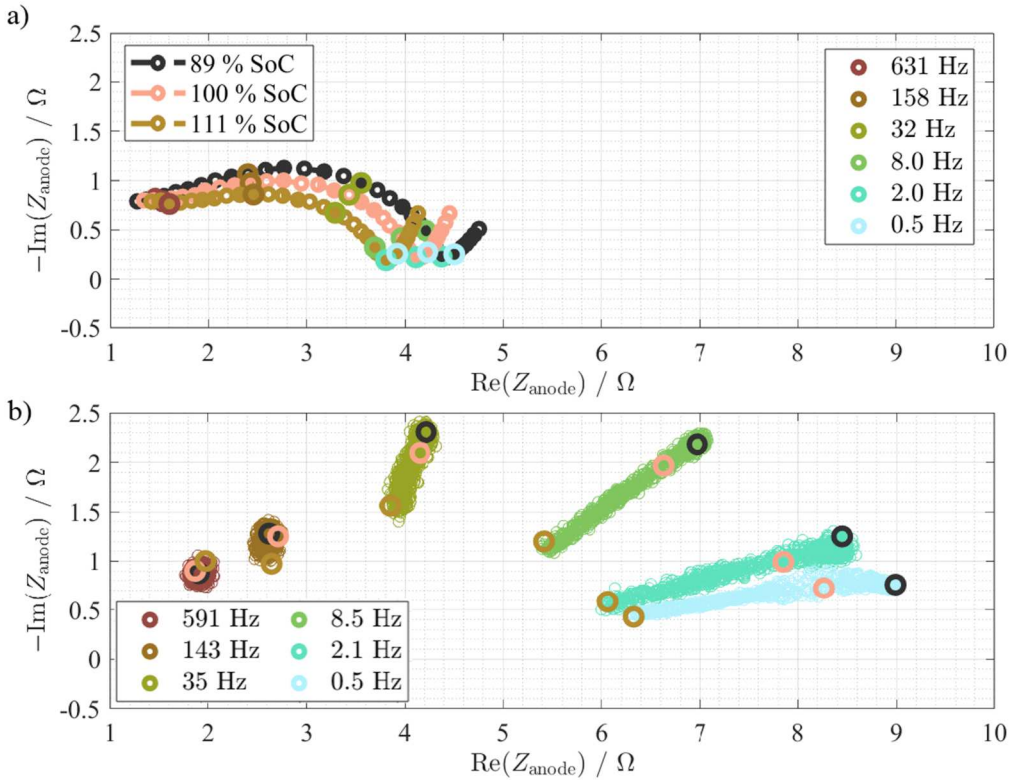

Figure 6. Ex-operando EIS and operando impedance in the Nyquist plot. Figure (a) shows the ex-operando EIS for three different SoC from intercalation to LD onset to advanced LD. Six frequency points that are similar to the recorded operando impedance frequencies are color-coded. Figure (b) shows the course of the operando impedance frequencies in the same SOC range from 89 % to 111 %. The three SoCs of the corresponding ex-operando measurement are color-coded with thick circles.

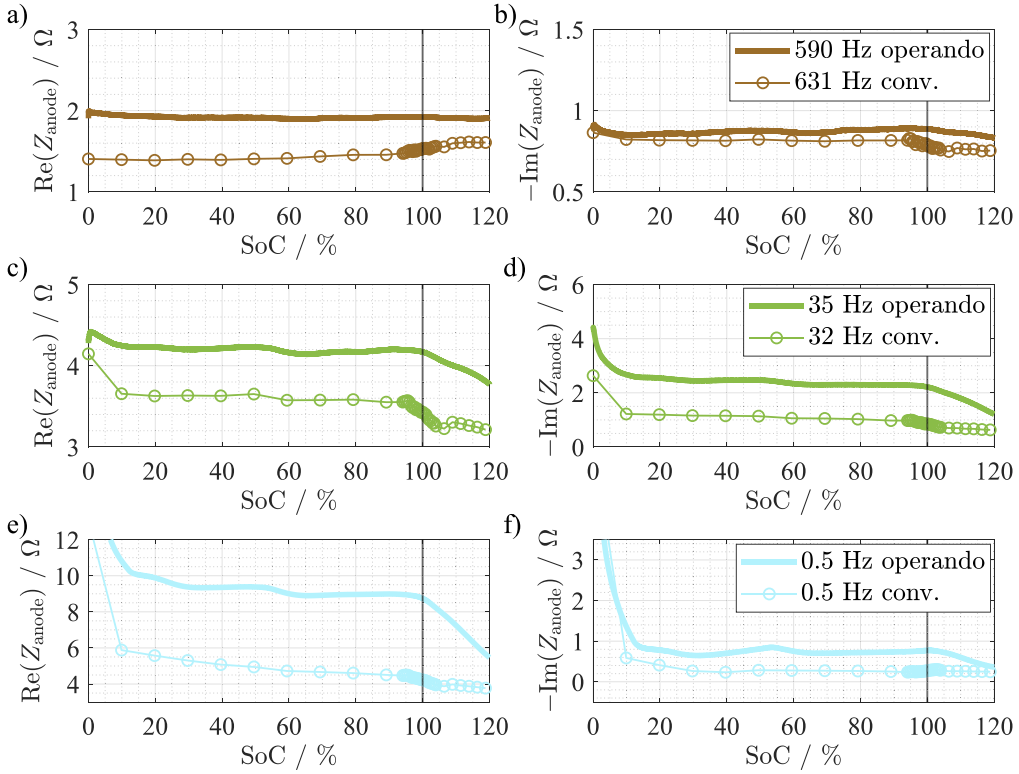

Figure 7. Comparison of EIS and operando impedance over SoC for three different frequencies.

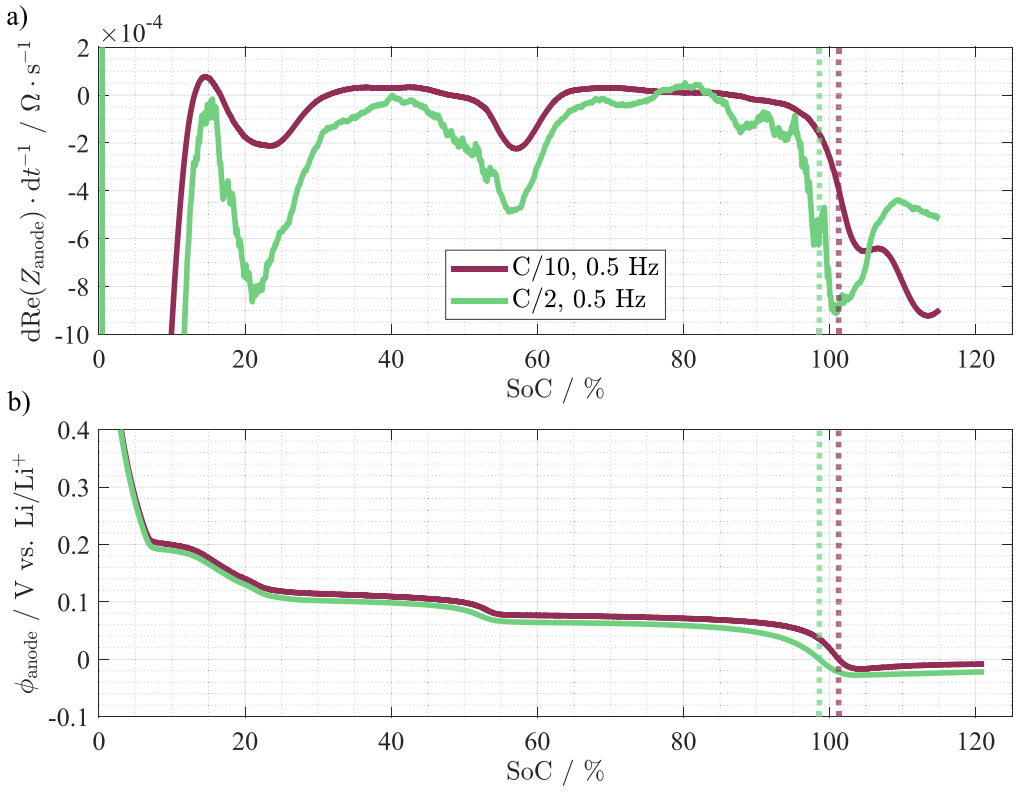

Figure 8. First derivative of the real part of the 0.5 Hz impedance for charging with C/10 in comparison to charging with C/2 in (a). Anode potential vs Li/Li$^+$ for the two cases in (b).

existing LD from a previous loading process. For the C/10 charge, as explained above, a sharp impedance drop at 96 % SoC is recognized as the onset of LD. When charging with C/2, an initial drop in impedance can already be perceived at 82 % SoC, before the derivative of the impedance curve drops very sharply at 95 % SoC. This behavior suggests that LD begins to occur in some particles as

early as 82 % SoC, potentially due to increasingly inhomogeneous lithiation fronts across the electrode thickness, before becoming more pronounced or predominant at 95 % SoC throughout the electrode. To make sure that no LD occurs at all, a charge limit for C/2 case would have to be set at 82 % SoC. If some LD can be tolerated, the limit can be set at 95 % SoC. Limited LD can be tolerated under the assumption that LD is partially reversible and can be stripped again in an immediately following discharge process. For a comprehensive assessment of the charging limits, the same experiment has to repeated for a combination of different C-rates and temperatures. In order to validate these results, the anode potential can be observed in experimental cells with reference electrode measurement. As can be seen, the anode potential reaches a value of 0 V vs Li/Li^+ earlier at the increased C-rate of C/2. This is due to the higher current density that increases the overpotentials at the anode, initiating LD at lower SoCs. In addition, the potential drop at approx. 100 % SoC, which indicates complete lithiation to LiC_6, is less pronounced at C/2 and begins at an earlier SoC than in the C/10 charging case. This behavior confirms the assumption of a less homogeneous lithiation.

Conclusion and Outlook

This work presents an experimental approach to explain the influence of parasitic lithium deposition in graphite electrodes on impedance measurements. Conditions from intercalation of Li ions into graphite via the onset of LD to exclusively LD are created to link impedance behavior directly to the three phases of LD for the first time. To achieve this objective, experimental anode-limited cells with an overdimensioned cathode equipped with a reference electrode are slowly overcharged while electrochemical impedance spectra and operando impedance measurements are conducted. Operando impedance measurements show a drop in impedance in characteristic frequencies during charging when LD occurs. As the operando measurements violate the LTI criteria, the results are compared with ex-operando impedance spectroscopy to verify the validity and cause of the impedance drop. The EIS measurements at different conditions (intercalation - LD onset - ongoing LD) are analyzed for changes in the Nyquist plot and by a process identification using a DRT analysis. In the Nyquist plot the onset of LD is visible in a reduction of the depressed semicircle's height and width due to the parallel LD reaction, which reduces the current density of the intercalation reaction and therefore the charge-transfer resistance. By interpreting the results of the DRT analysis, the change in SEI resistance during the onset and progression of LD can be monitored as another fingerprint of LD. The comparison of the impedance spectra with the operando impedance data confirms that the impedance drop in the charge transfer frequency region can be clearly attributed to LD. The experimental approach of the operando impedance is well suited to create parameter maps for current limits for fast charging. The precise determination of the LD onset allows a more precise control of currents during charging to avoid LD and to prevent the charging current limit from being set too conservatively. This not only extends the service life of the cell, but also significantly increases operational safety and the fast-charging capability. In future works, the results of the EIS experiments will be used to parameterize electrochemical models of lithium-ion cells including the side reactions of lithium deposition and stripping, enabling the simulation and prediction of electrochemical processes during charging and discharging. In particular, this approach allows for the calculation of current distributions within the cell during the occurrence of LD.

Acknowledgments

Support by the BayBatt Cell Technology Center, funded by the Deutsche Forschungsgemeinschaft (DFG, German Research Foundation) - INST 91/452-1 LAGG, is gratefully acknowledged. In order to improve the readability and language quality of this manuscript, ChatGPT by OpenAI and Writer by DeepL were utilized during the writing process. It is important to note that the content and ideas presented in the manuscript were not generated by these language models and the authors take full responsibility for the content. The color palette used in this report was developed by Crameri et al.[65] and is publicly available on Zenodo (https://doi.org/10.5281/zenodo.8035877).

Appendix

Appendix A: Full cell, anode and cathode impedance.—To assess whether the impedance spectra measured using the reference ring setup are free from measurement artifacts, the impedance spectra of both the electrodes are recorded and the full cell impedance is calculated. They are shown in Fig. A.1.

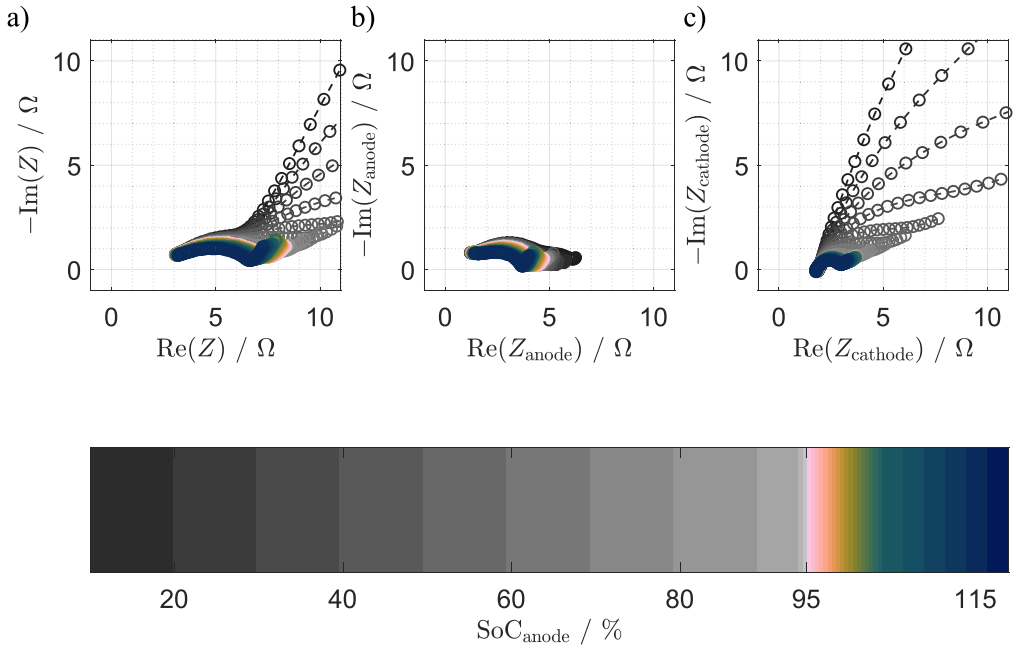

Figure A·1. Nyquist plots of the full cell impedance (a), anode impedance (b) and cathode impedance (c) of the experimental cell shown in Fig. 2 in the main body of the paper for different SoCs in a frequency range between 1.0 kHz and 0.1 mHz. The color map indicates the SoC, which is related to the capacity of the anode.

Appendix B: Nyquist plots of full cell over SoC.—While the primary focus of this work is on the anode processes, the full-cell impedance spectra are included in Fig. B.1 for completeness and to facilitate comparison with literature, where full-cell data is often reported. Due to the asymmetric electrode balancing used in this study, interpretation of the full cell impedance is limited and should be approached with caution. Nevertheless, the inclusion of this data allows for a qualitative alignment with previously reported full cell measurements and helps demonstrate that the observed impedance features are free of major artifacts. Furthermore, because of the low SoC of the cathode during the early stages of the measurement, no fully developed semicircle is visible in the recorded frequency range. Therefore, the analysis of the semicircle's width and height is shown only from an anode SoC of 90 % onwards.

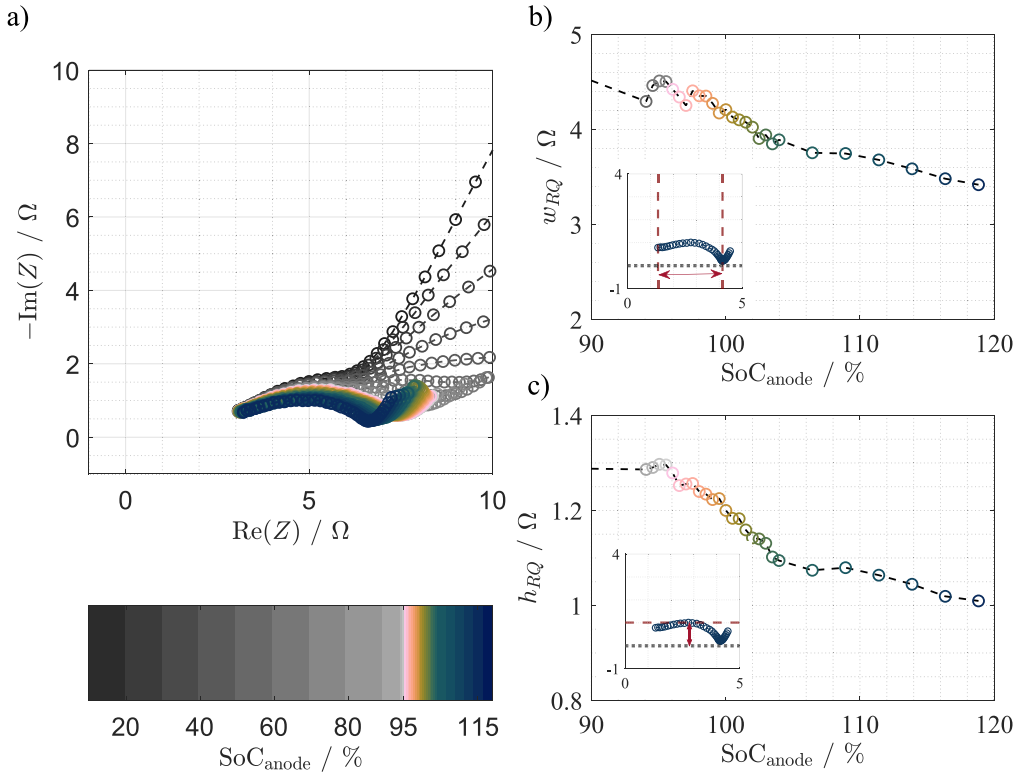

Figure B·1. Nyquist plots of the full cell impedance for different SoCs in a frequency range between 1.0 kHz and 0.1 mHz in (a). The color map indicates the anode SoC. Plot (b) show the width of the RQ-semicircle and plot c) the height of the RQ-semicircle. The inline plots in (b) and (c) illustrate the evaluation principle by showing how the width and height of the RQ-semicircle are determined.

Appendix C: Full cell and cathode DRT analysis.—To assess whether the DRT analysis is free from measurement artifacts the full cell and the cathode DRT analysis are shown in Figs. C.1 and C.2.

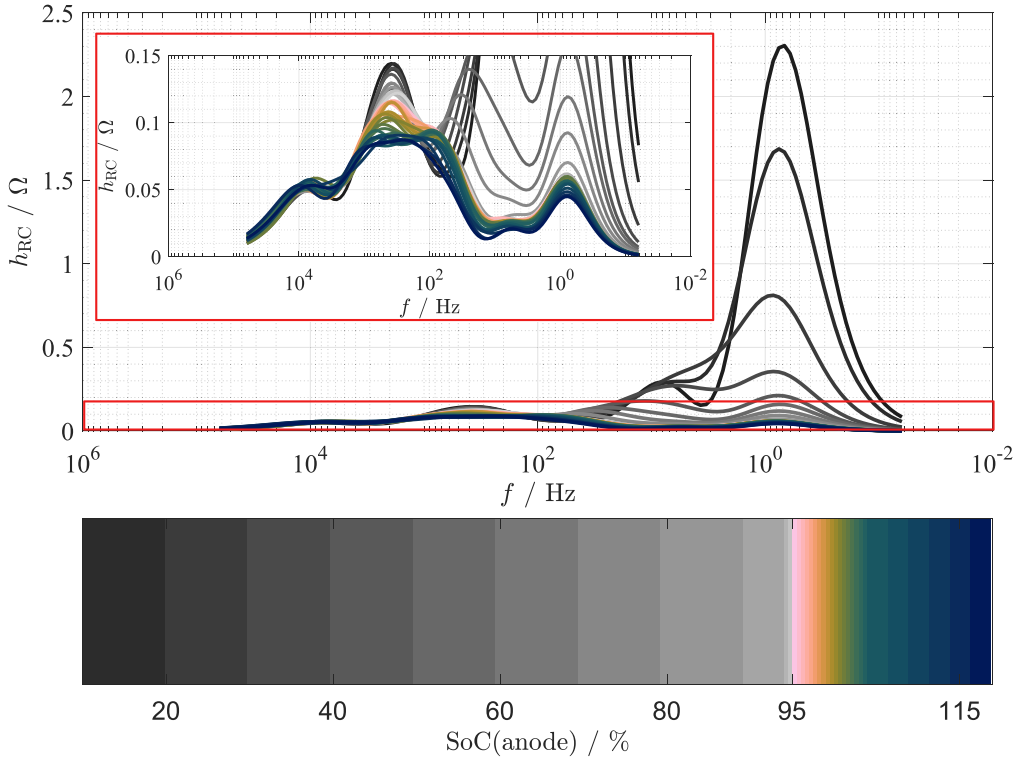

Figure C·1. DRT analysis of the full cell. The color map indicates the SoC, which is related to the capacity of the anode. The inlay plot shows a zoomed-in view of the region marked in red, providing a more detailed visualization of the peak structure.

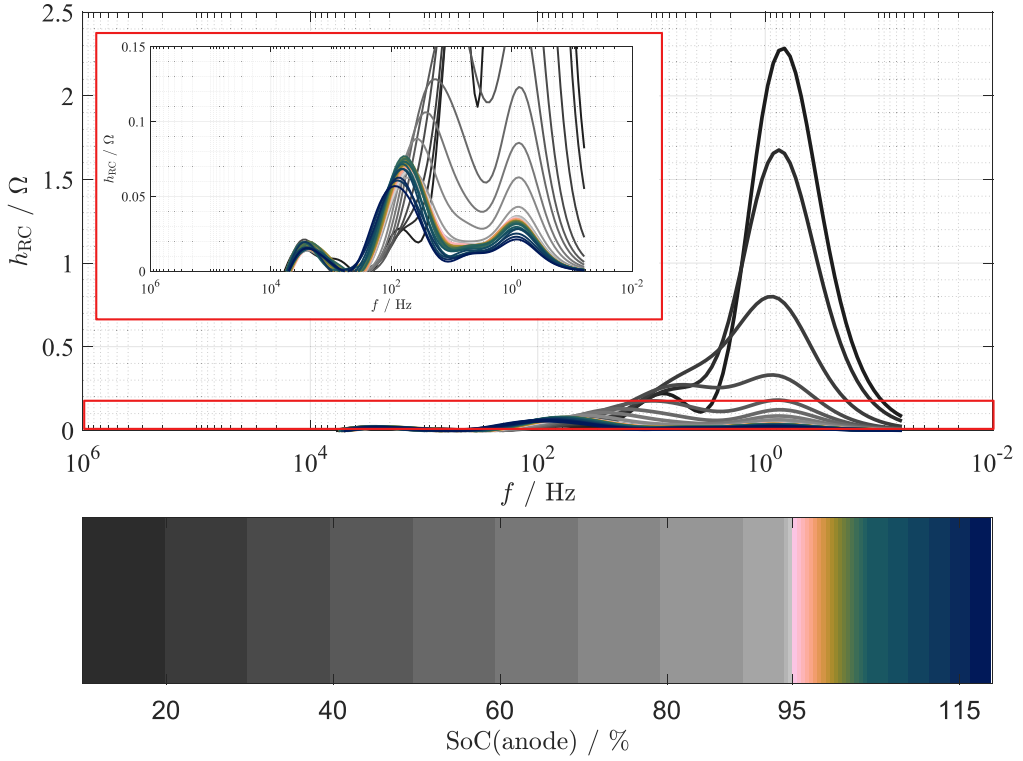

Figure C·2. DRT analysis of the cathode. The color map indicates the SoC, which is related to the capacity of the anode. The inlay plot shows a zoomed-in view of the region marked in red, providing a more detailed visualization of the peak structure.

Appendix D: Validation of anode impedance spectra with Kramers-Kronig test.—The validity of the measured anode impedance spectra is verified by performing an extended Kramers-Kronig test. An automated selection procedure was used to determine the number of RC elements, constrained to lie between 5 and 35. The residuals are shown in Fig. D.1.

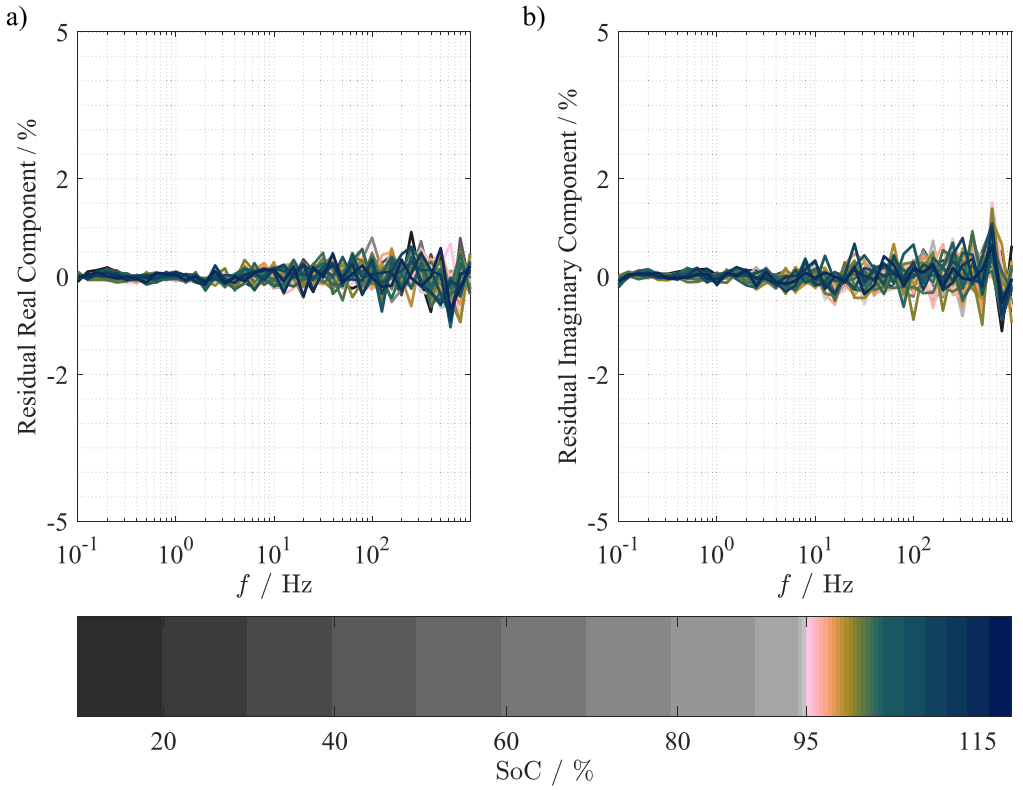

Figure D·1. Kramers–Kronig residuals of real part in (a) and imaginary part in (b) for the anode impedance spectra measured at different SoCs.

Appendix E: Operando impedance of full cell over SoC.—To facilitate comparison with existing literature, the operando impedance of the full cell are included and shown in Fig. E.1, as previous studies often report full cell measurements.

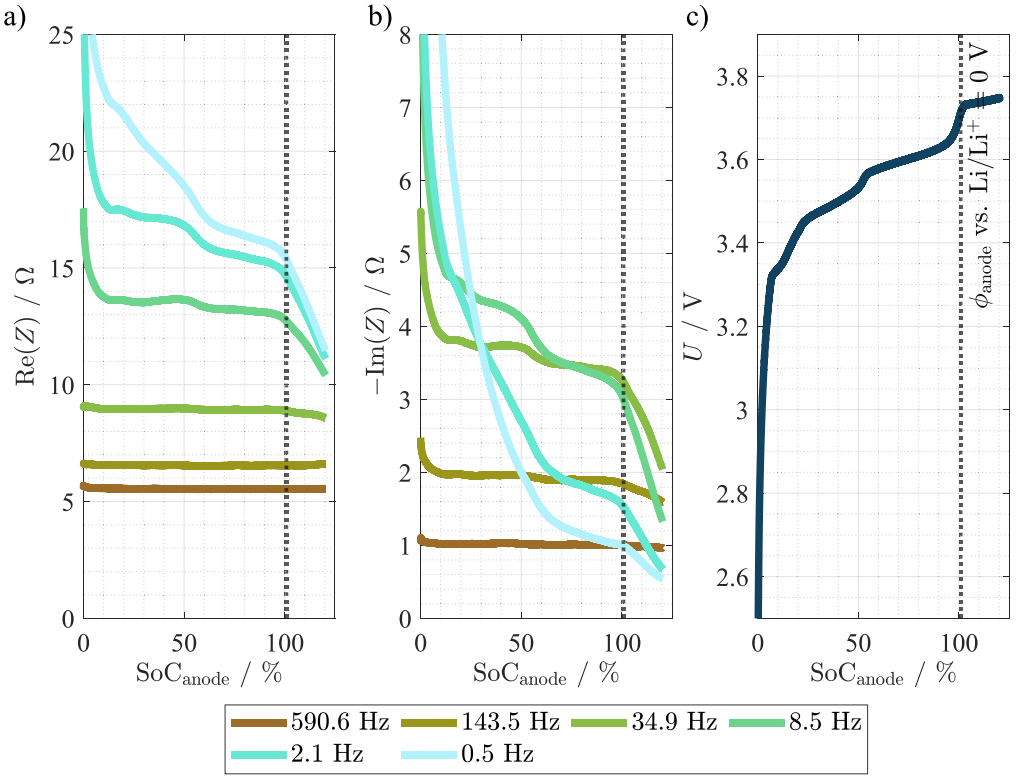

Figure E·1. Course of the real part and of the imaginary part of the full cell impedance of all tested frequencies in the operando impedance in (a) and (b). Plot (c) shows the full cell voltage during the measurement. The dashed lines marks the point where the anode potential vs Li/Li^+ reaches 0 V.

Appendix F: Nyquist plots of cell variation.—To demonstrate the reproducibility of the measurements presented in the Results and Discussion section, Nyquist data from two additional cells are shown in Figs. F.1 and F.2.

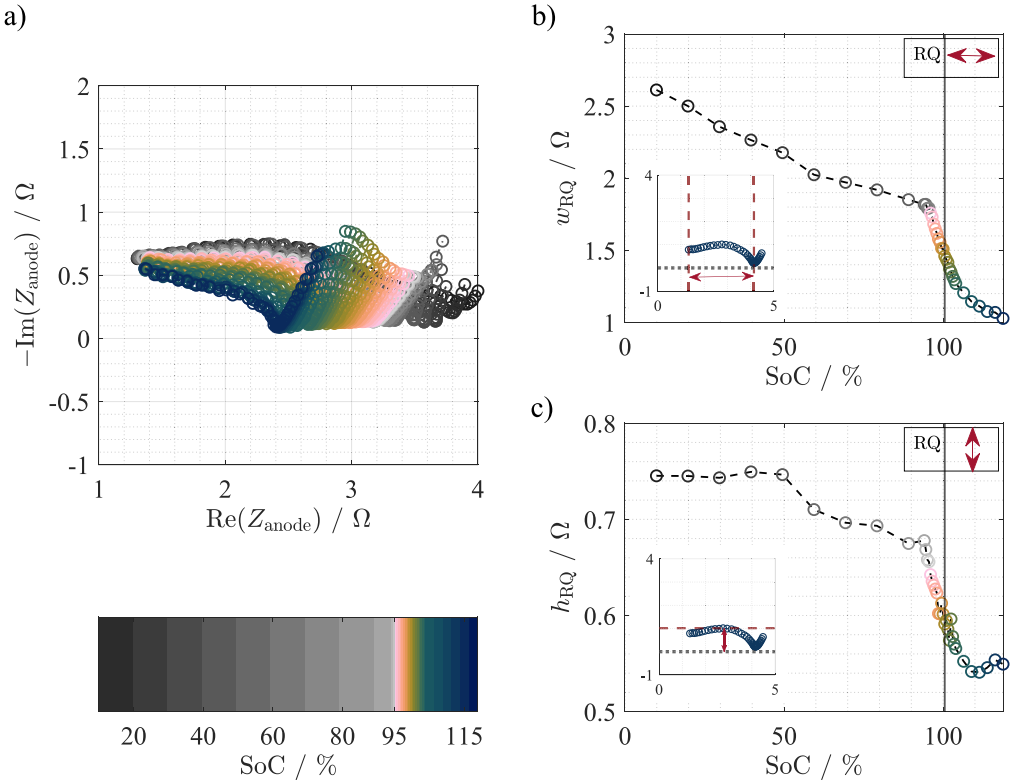

Figure F·1. Nyquist plots of the anode impedance of a second experimental cell for different SoCs in a frequency range between 1.0 kHz and 0.1 mHz in (a). The color map indicates the SoC of the anode. Plot (b) show the width of the RQ-semicircle and plot (c) the height of the RQ-semicircle. The solid line in plot (b) and (c) marks 100 % SoC. The inline plots in (b) and (c) illustrate the measurement principle by showing how the width w_{RQ} and height h_{RQ} of the RQ-semicircle are determined.

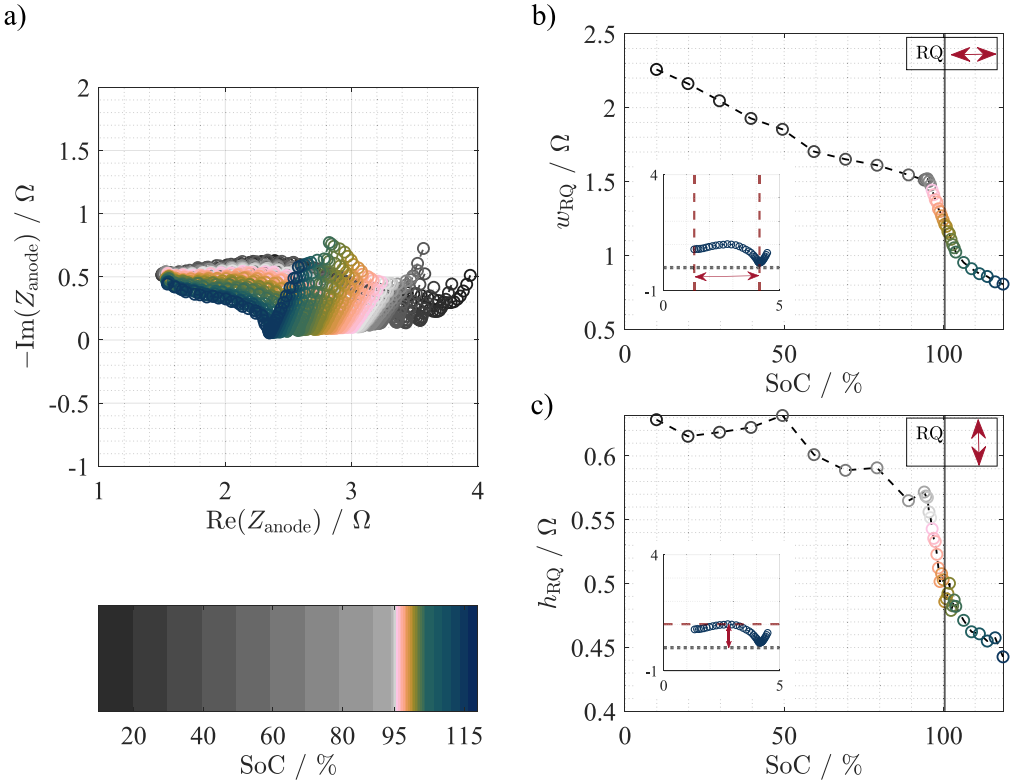

Figure F·2. Nyquist plots of the anode impedance of a third experimental cell for different SoCs in a frequency range between 1.0 kHz and 0.1 mHz in (a). The color map indicates the SoC of the anode. Plot (b) show the width of the RQ-semicircle and plot (c) the height of the RQ-semicircle. The solid line in plot (b) and (c) marks 100 % SoC. The inline plots in (b) and (c) illustrate the measurement principle by showing how the width w_{RQ} and height h_{RQ} of the RQ-semicircle are determined.

Appendix G: Anode operando impedance of cell variation.— To demonstrate the reproducibility of the measurements presented in the operando part of the Results and Discussion section, operando impedance measurement data from two additional cells are shown in Figs. G.1 and G.2.

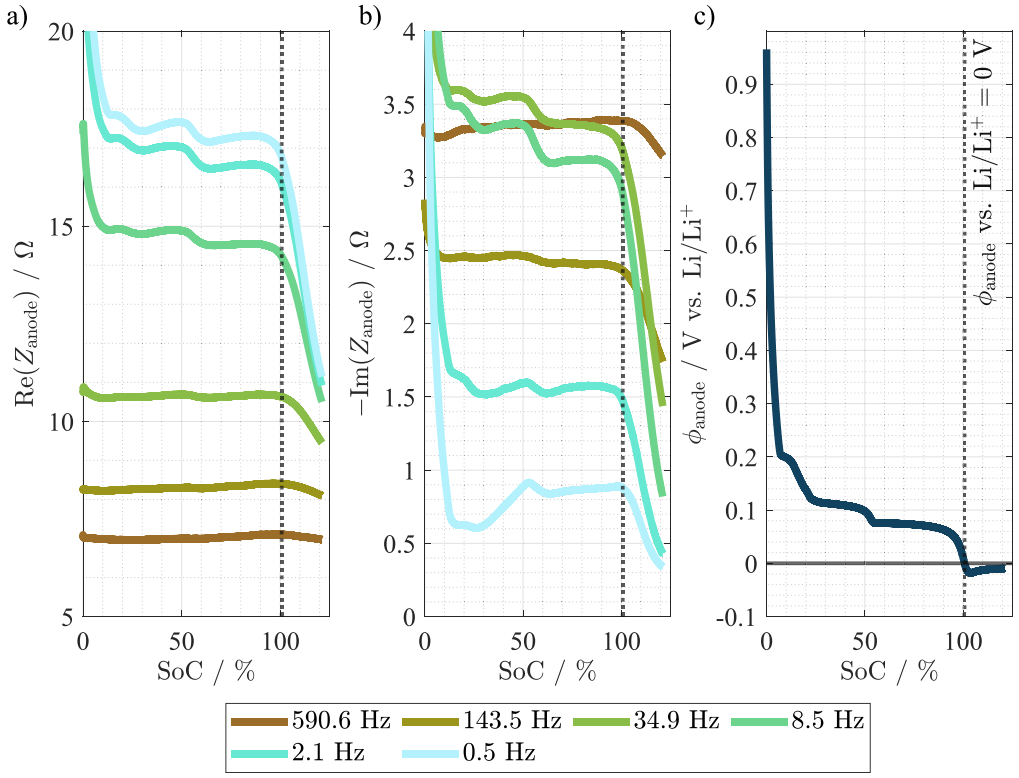

Figure G·1. Course of the real part and of the imaginary part of the operando impedance for a second cell in (a) and (b). Plot (c) shows the anode potential vs Li/Li$^+$ during the measurement. The dashed lines marks the point where the anode potential vs Li/Li$^+$ reaches 0 V.

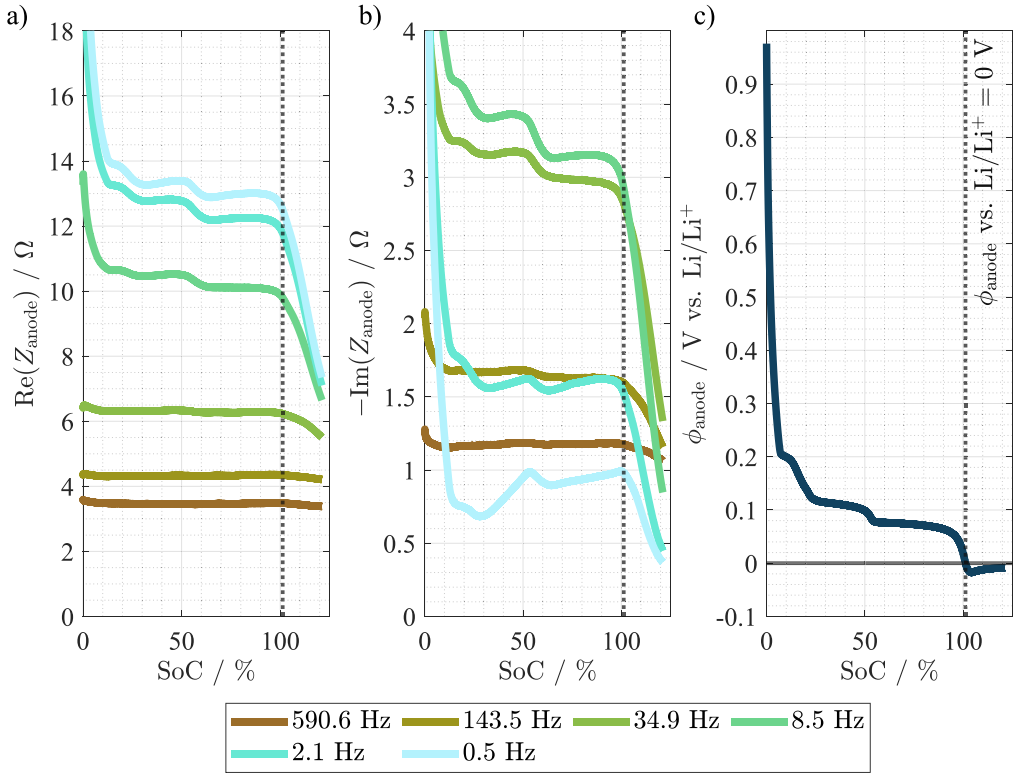

Figure G·2. Course of the real part and of the imaginary part of the operando impedance for a third cell in (a) and (b). Plot (c) shows the anode potential vs Li/Li$^+$ during the measurement. The dashed lines marks the point where the anode potential vs Li/Li$^+$ reaches 0 V.

ORCID

Andrea Kinberger https://orcid.org/0009-0009-1015-7961
Tom Rüther https://orcid.org/0000-0003-3696-5333
Leonard Jahn https://orcid.org/0000-0001-6496-4747
Michael A. Danzer https://orcid.org/0000-0002-4135-7263

References

1. A. Jossen and W. Weydanz, *Moderne Akkumulatoren Richtig Einsetzen* (Ubooks-Verlag, Neusäß and Berlin) 1st ed. (2006).
2. G. L. Plett, "Battery management systems." *Artech House Power Engineering and Power Electronics* (Artech House, Boston) vol 1 (2015).
3. M. S. Ziegler and J. E. Trancik, *Energy & Environmental Science*, **14**, 1635 (2021).
4. T. Rokicki, P. Bórawski, A. Bełdycka-Bórawska, A. Żak, and G. Koszela, *Energies*, **15**, 9 (2022).
5. A. G. Boulanger, A. C. Chu, S. Maxx, and D. L. Waltz, *Proc. IEEE*, **99**, 1116 (2011).
6. F. Katzer and M. A. Danzer, *Journal of Power Sources*, **503**, 230009 (2021).
7. F. Katzer, P. Mößle, M. Schamel, and M. A. Danzer, *Journal of Power Sources*, **555**, 232354 (2023).
8. N. Legrand, B. Knosp, P. Desprez, F. Lapicque, and S. Raël, *Journal of Power Sources*, **245**, 208 (2014).
9. S. Schindler, M. Bauer, M. Petzl, and M. A. Danzer, *Journal of Power Sources*, **304**, 170 (2016).
10. T. Waldmann, B. I. Hogg, and M. Wohlfahrt-Mehrens, *Journal of Power Sources*, **384**, 107 (2018).
11. T. Waldmann, M. Kasper, and M. Wohlfahrt-Mehrens, *Electrochimica Acta*, **178**, 525 (2015).
12. U. R. Koleti, A. Rajan, C. Tan, S. Moharana, T. Q. Dinh, and J. Marco, *Energies*, **13**, 3458 (2020).
13. J. C. Burns, D. A. Stevens, and J. R. Dahn, *J. Electrochem. Soc.*, **162**, A959 (2015).
14. C. Uhlmann, J. Illig, M. Ender, R. Schuster, and E. Ivers-Tiffée, *Journal of Power Sources*, **279**, 428 (2015).
15. M. Petzl and M. A. Danzer, *Journal of Power Sources*, **254**, 80 (2014).
16. Q. Liu, C. Du, B. Shen, P. Zuo, X. Cheng, Y. Ma, G. Yin, and Y. Gao, *RSC Adv.*, **6**, 88683 (2016).
17. J. Steiger, D. Kramer, and R. Mönig, *Journal of Power Sources*, **261**, 112 (2014).
18. F. Katzer, L. Jahn, M. Hahn, and M. A. Danzer, *Journal of Power Sources*, **512**, 230449 (2021).
19. Z. M. Konz, E. J. McShane, and B. D. McCloskey, *ACS Energy Lett.*, **5**, 1750 (2020).
20. U. R. Koleti, C. Zhang, R. Malik, T. Q. Dinh, and J. Marco, *Journal of Energy Storage*, **24**, 100798 (2019).
21. I. D. Campbell, M. Marzook, M. Marinescu, and G. J. Offer, *J. Electrochem. Soc.*, **166**, A725 (2019).
22. M. Bauer, M. Wachtler, H. Stöwe, J. V. Persson, and M. A. Danzer, *Journal of Power Sources*, **317**, 93 (2016).
23. L. Jahn, F. Katzer, and M. A. Danzer, *Journal of Power Sources*, **520**, 230870 (2022).
24. F. B. Spingler, W. Wittmann, J. Sturm, B. Rieger, and A. Jossen, *Journal of Power Sources*, **393**, 152 (2018).
25. B. Rieger, S. F. Schuster, S. V. Erhard, P. J. Osswald, A. Rheinfeld, C. Willmann, and A. Jossen, *Journal of Energy Storage*, **8**, 1 (2016).
26. A. Adam, E. Knobbe, J. Wandt, and A. Kwade, *Journal of Power Sources*, **495**, 229794 (2021).
27. Y. Chen, L. Torres-Castro, K. H. Chen, D. Penley, J. Lamb, M. Karulkar, and N. P. Dasgupta, *Journal of Power Sources*, **539**, 231601 (2022).
28. J. Kim, W. Lee, J. Seok, S. Park, J. K. Yoon, S. B. Yoon, and W. S. Yoon, *Cell Reports Physical Science*, **4**, 101331 (2023).
29. F. Grimsmann, T. Gerbert, F. Brauchle, A. Gruhle, J. Parisi, and M. Knipper, *Journal of Power Sources*, **365**, 12 (2017).
30. B. Bitzer and A. Gruhle, *Journal of Power Sources*, **262**, 297 (2014).
31. X. Zhang et al., *Journal of Energy Storage*, **108**, 115140 (2025).
32. T. Sun, Z. Li, G. Zhu, L. Wang, D. Ren, T. Shen, L. Lu, Y. Zheng, X. Han, and M. Ouyang, *Electrochimica Acta*, **496**, 144512 (2024).
33. M. Koseoglou, E. Tsioumas, D. Ferentinou, N. Jabbour, D. Papagiannis, and C. Mademlis, *Journal of Power Sources*, **512**, 230508 (2021).
34. A. Straßer, A. Adam, and J. Li, *Journal of Power Sources*, **580**, 233366 (2023).
35. F. Katzer, T. Rüther, C. Plank, F. Roth, and M. A. Danzer, *Electrochimica Acta*, **436**, 141401 (2022).
36. M. Dotoli, E. Milo, M. Giuliano, R. Rocca, C. Nervi, M. Baricco, M. Ercole, and M. F. Sgroi, *Batteries*, **7**, 46 (2021).
37. D. E. Brown, E. J. McShane, Z. M. Konz, K. B. Knudsen, and B. D. McCloskey, *Cell Reports Physical Science*, **2**, 100589 (2021).
38. J. P. Schmidt, A. Adam, and J. Wandt, *Batteries*, **9**, 97 (2023).
39. J. Keilhofer, F. Adam Dorau, H. C. Hsiao, B. Suthar, and R. Daub, *J. Electrochem. Soc.*, **171**, 110520 (2024).
40. J. Ulrich, A. Lindner, T. Brake, M. Winter, S. Wiemers-Meyer, A. Weber, and U. Krewer, *Journal of Power Sources*, **647**, 237358 (2025).
41. U. R. Koleti, T. Q. Dinh, and J. Marco, *Journal of Power Sources*, **451**, 227798 (2020).
42. Z. Jiang, J. Wang, H. Li, B. Luo, W. Wu, X. Wang, H. Dai, J. Jiang, and X. Wei, *Batteries*, **10**, 410 (2024).
43. T. Rüther, W. Hileman, G. L. Plett, M. S. Trimboli, and M. A. Danzer, *J. Electrochem. Soc.*, **171**, 060508 (2024).
44. C. Plank, T. Ruther, and M. A. Danzer, "Detection of non-linearity and non-stationarity in impedance spectra using an extended kramers-kronig test without overfitting." *2022 International Workshop on Impedance Spectroscopy (IWIS)* (IEEE) (2022).
45. C. Plank, T. Rüther, L. Jahn, M. Schamel, J. P. Schmidt, F. Ciucci, and M. A. Danzer, *Journal of Power Sources*, **594**, 233845 (2024).
46. V. Yrjänä and J. Bobacka, *Electrochimica Acta*, **504**, 144951 (2024).
47. B. A. Boukamp, *J. Electrochem. Soc.*, **142**, 1885 (1995).
48. M. Schönleber, D. Klotz, and E. Ivers-Tiffée, *Electrochimica Acta*, **131** (2014).
49. M. A. Danzer, *Batteries*, **5**, 53 (2019).
50. M. Hahn, S. Schindler, L. C. Triebs, and M. A. Danzer, *Batteries*, **5**, 43 (2019).
51. T. Paul, P. W. Chi, P. M. Wu, and M. K. Wu, *Sci. Rep.*, **11**, 12624 (2021).
52. A. Maradesa et al., *Joule*, **8**, 1958 (2024).
53. E. Barsoukov and J. R. Macdonald, *Impedance Spectroscopy* (John Wiley & Sons, Inc., Hoboken) (2005).
54. N. Hallemans, W. D. Widanage, X. Zhu, S. Moharana, M. Rashid, A. Hubin, and J. Lataire, *Journal of Power Sources*, **547**, 232005 (2022).
55. M. Schönleber, C. Uhlmann, P. Braun, A. Weber, and E. Ivers-Tiffée, *Electrochimica Acta*, **243**, 250 (2017).
56. X. Chen, L. Li, M. Liu, T. Huang, and A. Yu, *Journal of Power Sources*, **496**, 229867 (2021).
57. S. Gantenbein, M. Weiss, and E. Ivers-Tiffée, *Journal of Power Sources*, **379**, 317 (2018).
58. T. Rüther, C. Plank, M. Schamel, and M. A. Danzer, *Applied Energy*, **332**, 120514 (2023).
59. M. Heß and P. Novák, *Electrochimica Acta*, **106**, 149 (2013).
60. J. Asenbauer, T. Eisenmann, M. Kuenzel, A. Kazzazi, Z. Chen, and D. Bresser, *Sustainable Energy & Fuels*, **4**, 5387 (2020).
61. T. Gao, Y. Han, D. Fraggedakis, S. Das, T. Zhou, C. N. Yeh, S. Xu, W. C. Chueh, J. Li, and M. Z. Bazant, *Joule*, **5**, 393 (2021).
62. Y. Chen, K. H. Chen, A. J. Sanchez, E. Kazyak, V. Goel, Y. Gorlin, J. Christensen, K. Thornton, and N. P. Dasgupta, *Journal of Materials Chemistry A*, **9**, 23522 (2021).
63. K. Leung, F. Soto, K. Hankins, P. B. Balbuena, and K. L. Harrison, *The Journal of Physical Chemistry C*, **120**, 6302 (2016).
64. A. Tomaszewska et al., *eTransportation*, **1**, 100011 (2019).
65. Fabio Crameri, Grace E. Shephard, and Philip J. Heron, "The misuse of colour in science communication." *Nature Communications*, **11**, 5444 (2020).